Journal of Manufacturing Processes 131 (2024) 532–544

Contents lists available at ScienceDirect

Journal of Manufacturing Processes

journal homepage: www.elsevier.com/locate/manpro

Examining the impact of tool taper angle in Al-Si tube manufacturing by friction stir extrusion

Parviz Asadi [a,b], Mostafa Akbari [c], Tomasz Sadowski [d,*], Yaghuob Dadgar Asl [c], Naghdali Choupani [b], Fevzi Bedir [b]

[a] Advanced Materials Processing and Modeling Lab., Department of Mechanical Engineering, Faculty of Engineering, Imam Khomeini International University, Qazvin, Iran
[b] Department of Mechanical Engineering, Engineering Faculty, Gebze Technical University, 41400 Gebze, Kocaeli, Turkiye
[c] Department of Mechanical Engineering, Technical and Vocational University (TVU), Tehran, Iran
[d] Department of Solid Mechanics, The Lublin University of Technology, Nadbystrzycka 40 Str., 20-216 Lublin, Poland

ARTICLE INFO

Keywords:
Friction stir extrusion
Tool shape
Force
Material flow
Strain
Strain rate
Compressive strength

ABSTRACT

This study employed Friction Stir Extrusion (FSE) on the LM13 aluminum alloy to fabricate tubes using three distinct tool head designs: cylindrical, 30° taper, and 60° taper profiles. A comprehensive analysis of the microstructures and mechanical properties of the resulting samples was performed. A numerical study was conducted to model the process dynamics, focusing on temperature and strain distributions, material flow patterns, and the evolution of force, torque, strain, and strain rate. Findings indicated that the axial force with the cylindrical tool was 4–5 times greater than with tapered tools, while forces for the 30° and 60° taper tools were comparable. The 30° taper tool generated the highest strain value of 280 mm/mm, which significantly enhanced the mechanical strength of the pipe up to 139 MPa while it was 85 MPa in the base metal. However, the cylindrical tool had a much higher average strain rate of around 40 1/s, compared to below 10 1/s for the tapered tools, yet it was less effective at reducing porosity and breaking Si particles due to insufficient strain. Additionally, material flow patterns differed: with the cylindrical tool, flow moved from the periphery to the center, while tapered tools directed flow from the center toward the pipe wall.

1. Introduction

Aluminum-Silicon (Al-Si) alloys are popular in industry due to their excellent strength-to-weight ratio, high corrosion resistance, good castability, and thermal conductivity [1,2]. These lightweight alloys are ideal for applications requiring weight reduction and possess good wear resistance and thermal stability for high-temperature and abrasive conditions [3,4]. Their versatility and cost-effectiveness make them widely used in the automotive and aerospace sectors [5]. Aluminum alloy LM13, known as A413.0, is a common Al-Si casting alloy praised for its outstanding castability, high fluidity, and excellent corrosion resistance. While it offers good machinability and weldability, LM13 is prone to hot cracking during solidification [6,7], which can complicate certain casting processes, yet its favorable properties ensure its versatility in engineering applications.

Friction Stir Extrusion (FSE) is an innovative solid-state process that uses a rotating tool to mix and heat material within a mold [8], allowing for extrusion either between the tool and mold for tubes or through a central orifice for wire manufacturing [9–12]. Buffa et al. [13] conducted experiments and numerical analyses on how tool rotation and force affect the mechanical properties and microhardness of thin aluminum wires, noting that a tapered shoulder shape enhances solid bonding. They found that insufficient extrusion force can lead to insufficient strain or hot cracking, while excessive force reduces Specific Energy Consumption (SEC), improving the process's efficiency. Swarnkar et al. [14] used FSE to produce bimetallic tubes for automotive applications, achieving void-free bonding between the substrate and cladding through diffusion and testing various material combinations for feasibility.

The design of the rotating tool is vital for the success and efficiency of the FSE process. Its geometry, material composition, and surface features impact heat generation, material flow, and mechanical mixing. An optimized tool enhances heat input, facilitates stirring, and ensures uniform plastic deformation, leading to improved grain refinement and

* Corresponding author.
E-mail address: t.sadowski@pollub.pl (T. Sadowski).

https://doi.org/10.1016/j.jmapro.2024.09.047
Received 24 June 2024; Received in revised form 10 September 2024; Accepted 12 September 2024
Available online 19 September 2024

mechanical properties of the extruded product [15]. Additionally, tool design affects process stability, wear, productivity, and the force and strain applied during FSE. Properly managing these factors is essential for achieving high-quality, defect-free extrusions. Optimal force and strain are crucial for uniform material flow and effective mixing; insufficient levels may result in poor bonding and defects [16,17], while excessive force can cause adhesion to the tool and overheating, compromising product quality and stability [18]. Thus, controlling force and strain in FSE is critical for producing components with enhanced performance and integrity.

The Finite Element Method (FEM) is a powerful tool for simulating material flow, force, strain, strain rate, and temperature in the FSE process [19,20]. Validating FEM outcomes with empirical results enhances understanding of FSE mechanisms and enables forecasting of factors such as geometry, plunging speed, and tool rotational speed, ultimately optimizing process parameters for desired product properties. Baffari et al. [21] investigated FSE complexities through both experimental and numerical analyses, aiming to relate simulation results to experimental observations. They used a copper marker for clarity and employed thermo-mechanically coupled 3D Lagrangian modeling, verifying it by comparing temperature profiles. Their findings highlighted that integrating experimental and modeling data helps reconstruct the intricate material flow in FSE. Asadi et al. [10] developed a simulation model for FSE focused on brass wire production, using the Coupled Eulerian-Lagrangian (CEL) method and validating it through experiments. Their study examined the impact of process parameters, such as tool rotation and penetration speeds, on material movement, temperature, and strain contours. They found the highest strain and temperature near the tool-product interface but away from the tool axis, noting that while process parameters minimally affected material flow, it typically exhibited a conical helix pattern.

While some valuable works have examined the impact of tool design on the FSE process, there is a significant interest in studying the effects of tool head angle on various aspects such as microstructure, mechanical properties, temperature and strain distribution, material flow, as well as force and torque. In this study, the effect of taper angle on temperature

Fig. 1. (a) Schematic presentation of FSE process sequences (b) the fabricated tube inside the mold while the mold half is taken off, (c) the initial section of the pipe is cut as scrap and the rest will be used: (d) the compression test specimen sliced from the tube upside, and (e) the rest of pipe prepared for metallographic investigations.

and force during the process was explored. Three tools, including cylindrical and conical ones with cone angles of 30 and 60°, were used. The FEM model, developed based on the cel technique, was employed to investigate the impact of tool head design on force and temperature. Subsequently, extruded samples were produced using the designed tools. The mechanical properties and microstructural characteristics of the resulting tubes are assessed through diverse characterization methods, including Optical Microscopy (OM), Scanning Electron Microscopy (SEM), and compression testing.

2. Experimental procedure

The process of production consists of two main apparatuses: a rotating tool and a mold. Initially, a cylindrical primary ingot, with a diameter the same as the mold cavity, is positioned inside the mold (Fig. 1a). A tool made of non-consumable steel is used in the FSE process. The tool initiates rotation and plunges into the primary ingot, while frictional preheating ignites assisting to easier penetration of the tool. The pasty metal is then extruded upward as the tool rotates and descends. The mold and rotating tool are involved in the flow of it, resulting in the formation of a tube. During this stage of the process, the tool experiences high pressure, resulting in the transfer of a significant load to the spindle of the machine. After reaching a preordained depth and forming a tube of a certain length, the tool is then pulled back. Subsequently, the resulting tube is removed from the mold. Various stages of the friction stir extrusion are depicted in Fig. 1a. The tube produced is presented in Fig. 1b, while the process of preparing samples for compression and metallographic tests is shown in Figs. 1c-1e.

This research study utilized specific materials and tools in the manufacturing process. The mold was made from H13 hot-work steel, while the FSE tool was crafted from W360 hot-work steel, featuring an internal cavity of 25 mm in diameter and 100 mm in depth. Three tools were employed, including cylindrical and conical shapes with cone angles of 30 and 60°. The tool's cylindrical diameter was 21 mm and it could plunge at most 95 mm. The bottom diameter of conical tools was 7.5 mm. The rotating tool comprised two main components: the head, which directly contacted the material and reached temperatures of 700 to 800 °C, and the holder, which connected the tool to the rotating axis and experienced lower heating compared to the tooltip.

The tool design allows for cost-effective head replacements when productivity declines. A plasma nitration coating enhances durability and reduces friction, significantly increasing surface hardness and decreasing material adhesion to the tool. This improves efficiency and tool longevity during production. For this research, specific process parameters were selected, including a rotational speed of 630 rpm and a plunging speed of 40 mm/min, deemed suitable for achieving the desired outcomes.

The chemical composition of commonly utilized Al-Si alloy in the automotive sector, LM13, was analyzed using emission spectrometry and presented in Table 1. The compression test, adhering to standard procedures, was performed at room temperature employing a Cometech universal machine for tensile and compression testing. The 25-mm-length compression test sample underwent to strain rate of 10^{-3} 1/s during the compression test, the completion image of which is illustrated in Fig. 1d.

An OM and a Field Emission Scanning Electron Microscope (FESEM) were used for microstructural examination. The tubes were cut perpendicular to their axis, and the cross-sections were polished using standard procedures. The polished samples were then etched with Keller reagent to enhance the visibility of their microstructural features.

Table 1
Chemical composition of as-cast LM13 aluminum samples (wt%).

Si	Fe	Mn	Cu	Zn	Ni	Mg	Al
12.2	0.5	0.4	0.8	0.4	0.8	0.3	Balance

3. Numerical model

Deform-3DTM software was utilized by the researchers to simulate the FSE process, which is widely recognized for simulating processes with substantial plastic deformation [22,23]. It was assumed that the workpiece is modeled as a rigid-viscoplastic material, the tool is assumed to be rigid, the friction factor between the workpiece and tool is constant, and the thermal characteristics of both the workpiece and tool are considered to be constant throughout the process.

The rigid visco-plastic finite element method is commonly used in metal forming simulations. This method is derived from the principle of variational stability, which leads to the formulation of nonlinear equations. These nonlinear equations can be solved using iterative techniques, such as the Newton-Raphson method or direct solution methods [24].

A mesh was formed using 150,000 tetrahedrally arranged elements to model the FSE tool as a rigid body. In addition, the material was divided into two regions with distinct mesh patterns. Fine meshes with a size of 0.7 mm were applied to the top section of the billet that experienced severe plastic deformation (as shown in Fig. 2). The aluminum alloy flow stress was characterized by a function that takes into account the playing factors such as strain rate, temperature, and plastic strain [22].

$$\overline{\sigma} = \overline{\sigma}(\overline{\varepsilon}.\dot{\overline{\varepsilon}}.T) \tag{1}$$

where σ denotes the flow stress, ε denotes the plastic strain; $\dot{\varepsilon}$, the strain rate, and T symbolizes the temperature. In this investigation, the frictional force is computed by employing the constant shear model as shown below:

$$f = mk \tag{2}$$

In this equation, *f, m,* and *k* symbolize the frictional stress, the shear friction factor, and the shear yield stress, respectively. A friction coefficient of 0.35 was assumed in this study.

In this study, the convective boundary condition for all tool's surfaces is defined as:

$$k\frac{\partial T}{\partial n} = h(T - T_{amb}) \tag{3}$$

where h represents the convection coefficient, T_{amb} is the ambient temperature, and n is the boundary's normal vector. The coefficient of convection for surfaces displayed to the environment is considered 20 W/(m^2.°C). The workpiece and the tool were exposed to the surrounding atmosphere at the ambient temperature of 25 °C. Moreover, the thermal properties of the H13 steel tool and LM13 samples are summarized in Table 2.

4. Results and discussions

The analysis includes the examination of tubes manufactured through FSE using three distinct tool head designs, in conjunction with the LM13 Base Material (BM), to assess mechanical and microstructural characteristics. A FEM simulation is employed for deriving the force, torque, strain, strain rate, and temperature profiles throughout the process, aiding in a thorough explanation of the observed properties in the FSE products. Furthermore, the flow of material depicted in the model outcomes is deliberated upon and contrasted by experimental data to explore the impact of tool design on numerical flow patterns, temperature and force profiles, as well as strain distribution.

4.1. Forming by FSE and its microstructural effects

A cross-sectional view of the processed specimens, revealing four zones along the tube's length is shown in Fig. 3a. The initial zone features the BM with a microstructure of unevenly dispersed needle-like

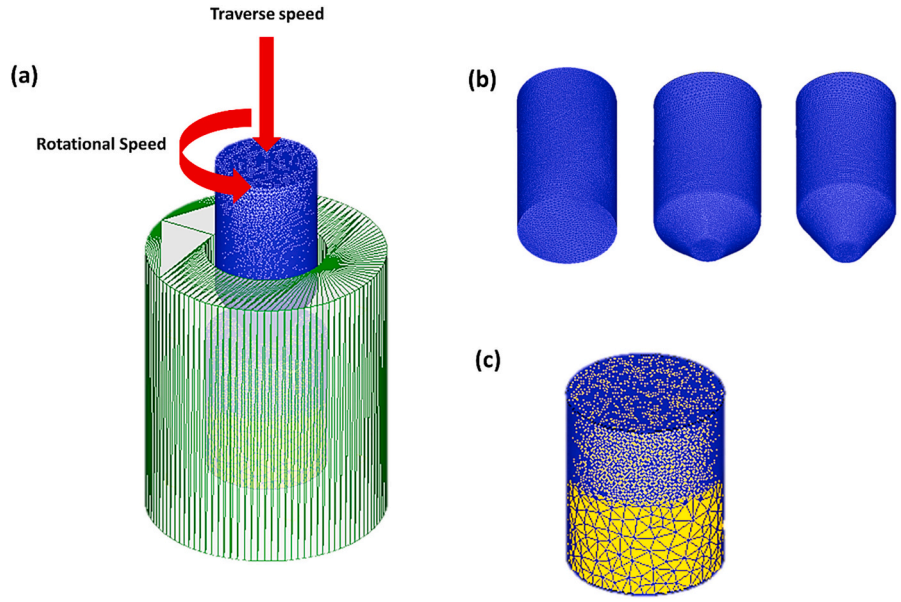

Fig. 2. The FSE (a) mold, (b) tool, and (c) workpiece prepared for the simulation model.

Table 2
Thermal properties of the LM13 alloy, mold, and tool.

Property	A356	Tool	FSE mold
Conductivity (W/m K)	151	24.5	24.5
Heat capacity (N/mm2°C)	2.4	4.5	4.5
Heat transfer coefficient between tool and workpiece (N/°C s mm2)	11	11	–
Heat transfer coefficient between mold and workpiece (N/°C s mm2)	11	–	11
Emissivity	0.25	0.7	0.7

silicon precipitates in the aluminum matrix. These large particles can reduce the mechanical properties of LM13, increasing brittleness due to stress concentration [25,26]. Voids are also noted in the base material, where the Si precipitates average 15 μm in size and have an aspect ratio of 4.9, influencing alloy properties.

While elongated precipitates can enhance strength and hardness by impeding dislocation motion, their needle-shaped tips can lead to increased crack susceptibility and reduced tensile properties [27]. Transforming these needle-like silicon particles into nearly spherical ones with lower aspect ratios can mitigate these issues, reducing stress concentration and enhancing isotropy and homogeneity in the alloy.

Using nearly spherical particles with reduced aspect ratios in aluminum alloys provides advantages such as lower crack propagation likelihood, improved tensile strength, and increased fracture elongation. Decreasing the aspect ratio while ensuring uniform distribution can enhance isotropic mechanical properties [23]. Techniques such as heat treatment, specialized solidification methods like melt spinning, and SPD approaches can convert needle-like silicon precipitates to nearly spherical ones [28–30].

The lengthwise cross-section of the fabricated specimens in Fig. 3a shows distinct zones and structural changes, with microstructures at points labeled b-e depicted in Figs. 3b-3e. Moving from the base material to the tooltip, a segment of metal experiences high strain and temperature, causing silicon to fragment into smaller particles and decrease its aspect ratio. This region is known as the Thermo-Mechanically Affected Zone (TMAZ), where, despite partial breakage, the precipitates maintain orientation toward the future shape of the Tube Wall (TW).

The area between the TMAZ and the tool head is called the Stir Zone (SZ). Fig. 4c shows the microstructure of the SZ, where silicon precipitates are fractured, with no needle-like formations present. Elevated temperatures and severe strain in the SZ may cause some precipitates to dissolve [31,32]. Significant material flow in this region removes needle-shaped silicon precipitates and voids from the base material, leading to improvements in the mechanical characteristics of the final product.

As the tool rotates and advances into the base material, it directs material toward the tube wall's taper section. Friction levels vary, with high friction between the tool and the inner tube wall and lower friction between the outer tube wall and the mold. The microstructure of the tube wall is characterized by a uniform distribution of small, round Si precipitates in the substrate, as shown in Fig. 3d.

The silicone precipitate size varies gradually in distinct regions of the manufactured specimens, decreasing in size from the base material to the thermo-mechanically affected zone and stir zone, and further to the tube wall. In the BM, the mean dimension of silicones is around 9.7 μm, whereas in the TMAZ, the particles are partially fractured, leading to an average size reduction of approximately 4.5 μm. The particle breakage progresses into the SZ, where primary Si particles are no longer evident, and the mean dimension decreases to nearly 2.7 μm. This plastic deformation and particle breakage extend beyond the conical part of the tool, resulting in a reduction in the silicone's mean dimension to about 1.8–2 μm in the tube wall (Fig. 3e). Simulation results would be beneficial in substantiating this phenomenon.

4.2. Temperature contours

The contours of temperature for the FSE samples, created using three different tool head designs, are illustrated in Fig. 4. The upper row of the image shows the entire pipe, while the middle row and lower row images demonstrate the longitudinal and radial cross-sections of the produced pipes.

Upon initial inspection, it is evident that when producing a similar pipe length, the temperature range is higher in the sample processed with the steeper taper angle (30°) for the tool head. This is attributed to the larger contact surface between the tool and the material being processed, resulting in increased frictional heat generation and subsequently higher peak temperatures in the material produced with the 30° taper head. These temperature variations among the different tools are expected to influence the material softening degree, material flow patterns, as well as the precipitate size within the structure of the fabricated

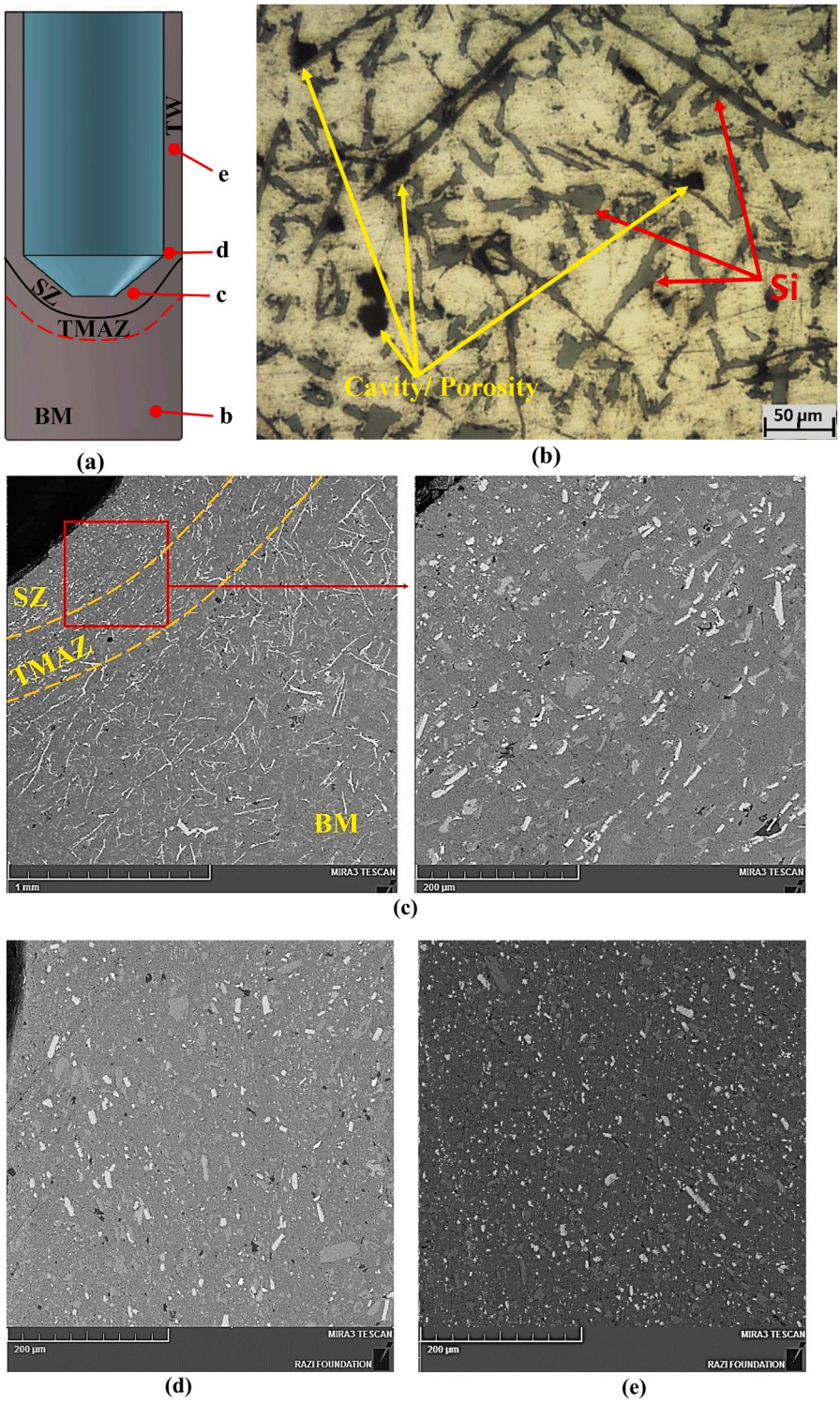

Fig. 3. (a) The lengthwise axis cross-section view of the FSE-produced tube, (b) OM showing the BM microstructure. SEM microstructural view of (c) tool taper head demonstrating SZ and TMAZ with two different magnifications, (d) the conjunction of taper section and tube wall, and (e) the center of the tube wall.

pipes.

When examining the longitudinal cross-section for the temperature contours (e.g., Fig. 4d), it is noteworthy that the peak temperatures do not occur around the conical head of the tool, as one might expect. Instead, it develops in a bit upper regions in which the materials have had greater frictional force and undergone increased strain. This leads to the generation of additional heat from frictional forces and plastic strains. The highest temperatures in these regions reach some values, ranging from 430 to 460 °C for the three different tool designs.

The interplay between a high strain and heat generation through friction within the FSE process will affect distinctly the produced alloy properties. One desirable outcome is that the extensive plastic deformation and high temperature in the stir zone cause the fragmentation of silicon precipitates and facilitate the formation of a more uniform structure.

Furthermore, elevated temperatures during the FSE process can

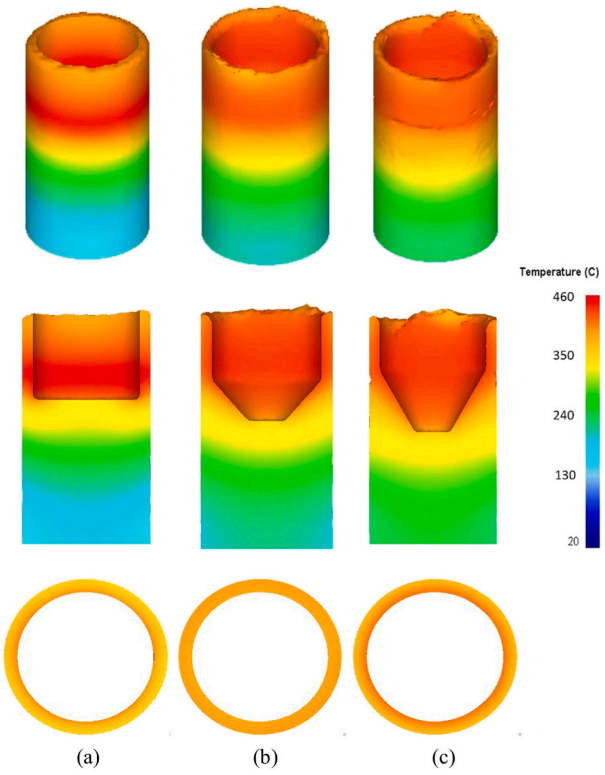

Fig. 4. Temperature distribution in the FSE samples of (a) cylindrical tool, (b) tool with 60° taper angle, and (c) tool with 30° taper angle.

facilitate the diffusion and dispersion of silicon particles within the aluminum matrix. This has a positive effect on the strength and malleability of the alloy, as it enhances the bonding between the Si particles and the matrix [33]. Consequently, it helps reduce porosity and irregularities present in the original cast material by promoting material softening and smoother material flow.

However, it is important to note that excessively high temperatures, along with excessive plastic deformation and material flow, can hasten the possibility of defect formation and ductility reduction [34]. The heat produced through friction also induces softening and thermal stresses, affecting the mechanical characteristics and microstructure.

To achieve the desired microstructural and mechanical characteristics in the FSE specimen, it is important to find the right balance between the frictional heat production and the plastic strain [35]. Through various experimental and simulation trials conducted at various plunging and rotational velocities, flawless specimens with satisfactory characteristics were obtained using a tool with a 30° taper angle, a plunging speed of 40 mm/min, and a rotational speed of 630 rpm. These optimized parameters yielded the desired outcome in terms of mechanical properties and microstructure.

4.3. Strain distribution

The strain distributions are compared for three tool designs in the lengthwise axis cross-sectional view of the specimen during different tool penetration steps in the FSE process in Fig. 5a. To show the details of strain distribution, the workpiece for each tool design is shown lonely without the tool and mold at the last step (Fig. 5b).

In all instances, the most significant level of strain occurs within the tube's inner layers, specifically 6–10 mm higher than the completion point of the conical section. This indicates that the intense plastic strain does not cease at the end of the conical section; rather, the most substantial deformation transpires beyond this juncture. It appears that the temperature peak is not reached immediately after at the conclusion of the conical region due to the combined effects of friction and heat generated by plastic deformation. This delay results in the peak temperature manifesting slightly further along the tube, as illustrated in Fig. 4. As temperature rises, the material becomes more pliable, leading to increased plastic deformation and strain.

In terms of strain and temperature patterns, the peak strain and temperature levels are observed 6–10 mm above the completion of the conical section. This is where the most significant breakage of Si particles occurs, particularly in the presence of the smallest particles (refer to Fig. 3e). It is important to note that both strain levels and temperatures increase as the materials traverse the conical section of the tool, which plays a crucial role in determining microstructural characteristics.

Upon comparing the effective strain among samples produced using three different tool designs, it is evident that the sample created with a 30° taper angle tool exhibits the highest level of strain on the material. This is attributed to the greater distance of material displacement within this particular tool. The detailed discussion of this phenomenon will be further explored using the point tracking technique. While the strain imparted on the material by the cylindrical tool is approximately 160, it rises to 230 and 270 for the tapered tools with 60° and 30° angles, respectively. Studies have shown that a higher level of strain applied during SPD processes results in the formation of a finer microstructure [36–38]. Moreover, in alloys featuring a dispersed second phase on the primary substrate, increased strain can lead to greater breakage of the second phase. Consequently, it is anticipated that the Si precipitates in LM13 alloy will become finer when subjected to the FSE process using a 30° taper angle tool.

4.4. Force and torque

The normal force on the cylindrical tool averages nearly 100 kN, significantly higher than the 15 kN for the taper head tools (Fig. 6a). This discrepancy poses risks to the cylindrical tool's lifespan and threatens the integrity of the mold and machinery.

The cylindrical tool's force history indicates a peak of nearly 200 kN upon initial contact with the workpiece, followed by a gradual decrease until the 6th second. Initially, the cold workpiece resists shaping, but as frictional heat softens the material, resistance decreases, allowing for easier forming. After the 6th second, the force rises again due to friction from the formed pipe moving in the channel between the rotating tool and stationary mold.

On the right side of Fig. 6a, the axial force histories of two tapered-head tools are compared, excluding the cylindrical tool for clarity. Although the tapered tools experience lower forces, they show a similar pattern: a high initial force, a decrease, and a rise toward the end. However, for the tapered tools, the initial force drop is minimal because their expanding contact surface counteracts the reduction in axial force from material softening.

In comparing the force history curves of the tapered tools, an initial expectation was that the axial force amount would be higher for the 60° tapered tool due to the lower temperature and material softening in this tool. Conversely, the axial force value for the 30° tapered tool is slightly higher, attributed to the larger contact surface area of this tool compared to the 60° tapered tool.

Showings the torque histories for three FSE tools, Fig. 6b reveals that the cylindrical tool torque is significantly higher, especially in the initial stages, due to its engagement with the entire cross-section from the start. In contrast, the tapered tools make initial contact with only a part of their cross-section, which gradually increases as they penetrate.

The torque value for the 30° tapered tool is also slightly higher than that of the 60° tapered tool because it sweeps more material. The relationship between swept material volume and material softening affects torque; while a larger volume requires more torque, softer material needs less. Thus, the volume of swept material is a key factor in tool design, particularly when comparing the 30° and 60° taper angles.

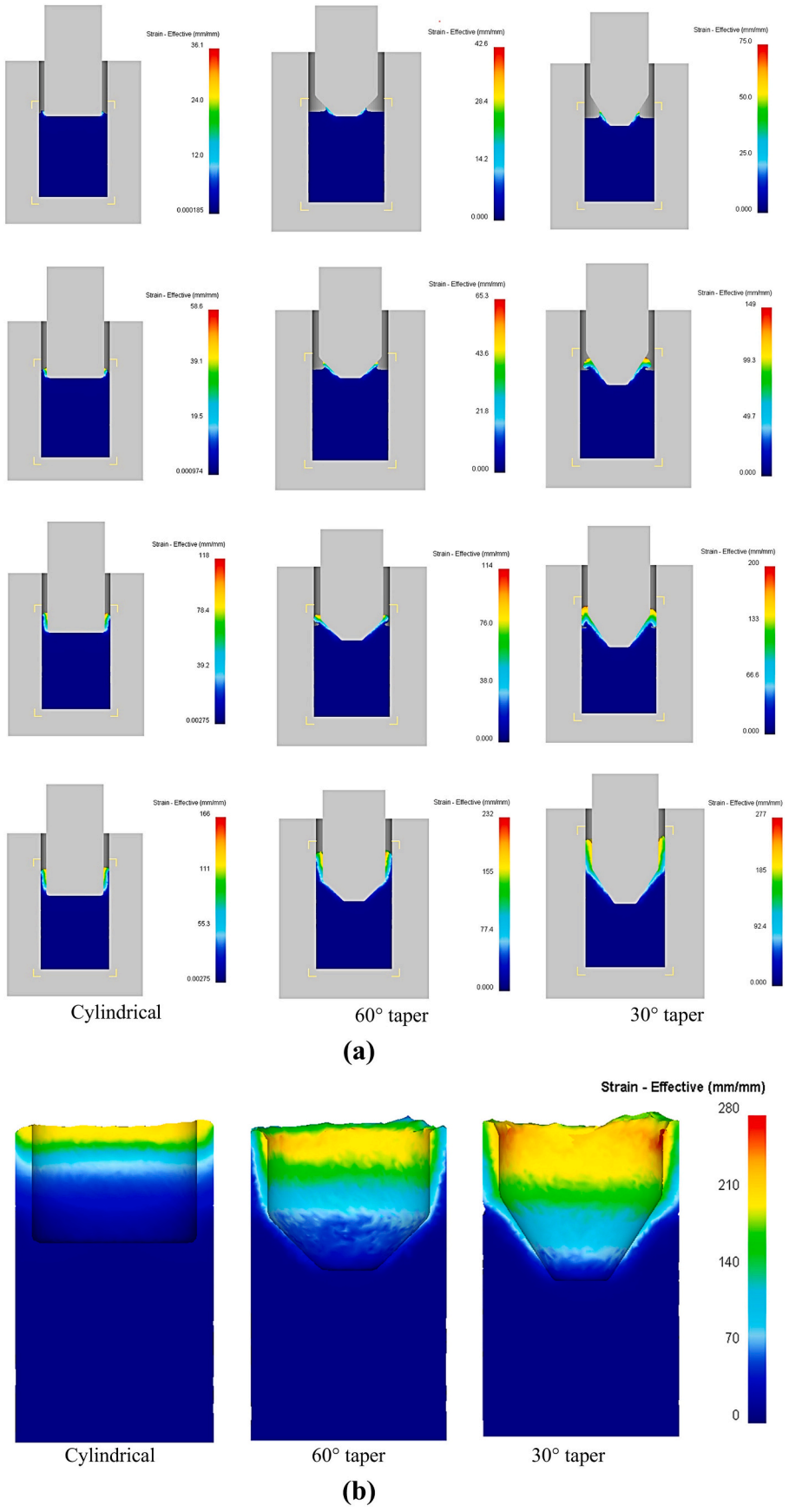

Fig. 5. Effective strain distribution in pipe production by FSE using different tool head designs of cylindrical, 60° taper angle, and 30° taper angle: (a) different steps of forming with the presence of tool, (b) last step without tool.

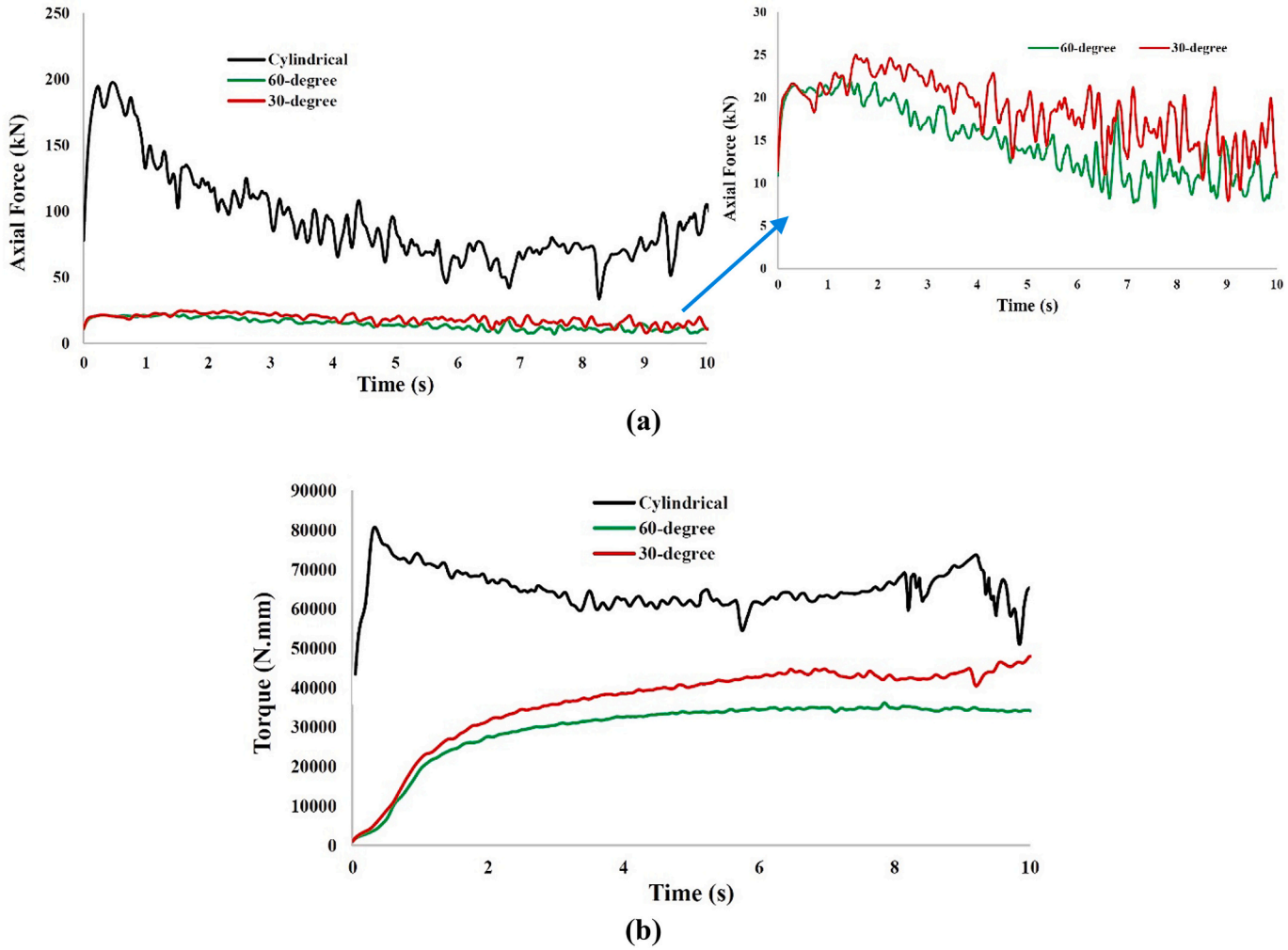

Fig. 6. (a) Axial force histories, and (b) torque histories, of three FSE tools employed in this study.

4.5. Material flow

As a critical factor in friction stir extrusion flow of material has a direct impact on the microstructure and mechanical properties of the product. During the FSE process, the frictional heat is generated by tool rotating and plunging actions, leading to metal softening and plastic flow [39]. This material flow plays a crucial role in breaking down silicon particles, ensuring their more uniform distribution within the aluminum matrix, and eliminating dendrites and cavities in the base metal structure [40]. As a result, it significantly enhances the alloy's mechanical characteristics. Thus, effective control of material flow is essential for optimizing FSE variables and achieving the requested microstructure and mechanical characteristics.

However, studying material flow in friction stir extrusion through experiments can be complex due to the intricate nature of the process. While the experiment provides valuable insights, it is sluggish, expensive, and may not result in the process comprehension. To complement experiments, thus, the utilization of numerical studies and simulation models are beneficial approaches, by predicting stress and strain fields as well as the material flow patterns. For example, the point-tracking capability of Deform^{3D} software allows for tracking material movement throughout the FSE process by strategically placing points along the tool path and observing their trajectories [21].

The observed characteristics of material movement within FSE are illustrated in Fig. 7, using three different tool head designs, shown in both side cross-section view and top view. Points P1-P3 are initially positioned on the radius of the initial ingot, with P1 near the outer edge and P2 and P3 positioned toward the center of the ingot, maintaining a 2 mm separation (Fig. 7a). Figs. 7b-7d depicts the trajectory of these points by progressive penetration of the FSE tool into the ingot, in various sequential stages using three FSE tools equipped with cylindrical and taper heads.

Upon comparing the material flow patterns of cylindrical and tapered head tools, a significant distinction in their material movement becomes apparent. In the cylindrical tool, points P1 to P3 move radially outward and sequentially enter the channel between the rotating tool and stationary mold to form the pipe wall. Conversely, in taper head tools, the material flow deviates from this pattern as P3 initiates a conical helical movement toward the channel before the other points. As a result, the order of entry into the pipe wall channel is P1, P2, and P3 for cylindrical tools, while for tapered tools, it is P3, P2, and P1. This difference in material flow patterns suggests a more intricate flow in samples produced with taper head tools compared to those from cylindrical tools, especially when the tool head design is a combination of cylindrical and conical shapes [41].

Alternatively, when examining the material flow patterns in tapered tools, a noticeable difference in the speed of point movement is observed between a 60° tapered tool and a 30° tapered tool. Specifically, when comparing the movement of point P3 in these tools from its initial position to the final step, it becomes apparent that the point moves faster when a 60° tapered tool is utilized. This increased speed may indicate a higher strain rate associated with the use of this tool. Conversely, the

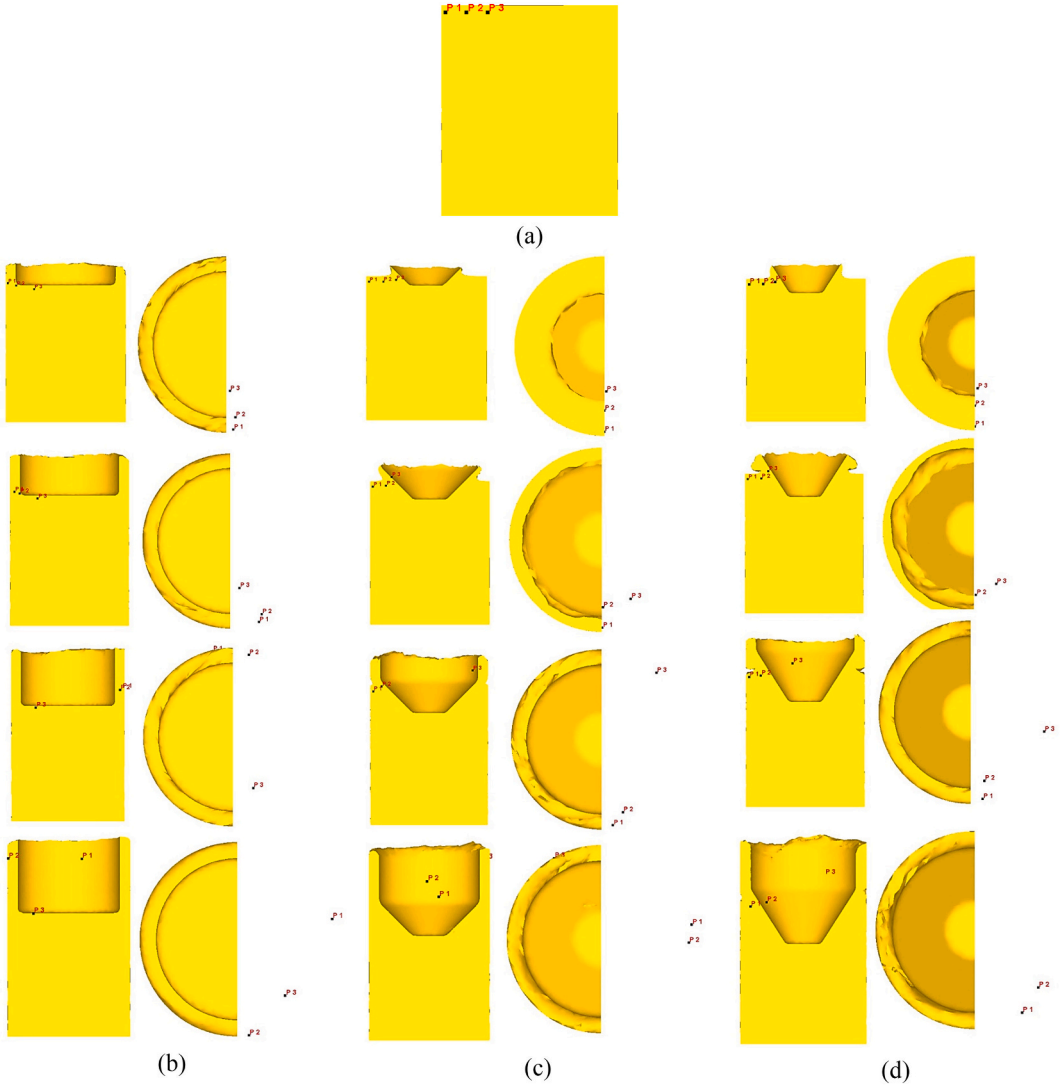

Fig. 7. (a) Initial locations of the P1-P3 points positioned on the initial ingot, and (b)-(d) the movement sequences of points while the rotation and penetration of the FSE tool. (b) cylindrical tool, (c) taper head tool with a 60° angle, and (d) taper head tool with a 30° angle.

path traveled by the point is longer when a 30° tapered tool is employed, suggesting a higher strain. Therefore, it is essential to analyze the strain and strain rate histories of the points to gain further insights into the material flow patterns.

The effective strain histories encountered by points P1-P3 during the utilization of different tool designs are illustrated in Fig. 8. These curves can be analyzed from two perspectives: the peak strain value and the timing and sequence of point movement.

Observing the sequence of points initiating movement reveals that, across all tools, point P3 is the first to enter the SZ and undergo strain, even with the cylindrical tool. While in the cylindrical tool, point P1 diverges by initially moving toward the pipe wall channel, it is ultimately point P3, similar to the other tools, that experiences the highest strain. Consequently, based on the peak strain values, it is evident that point P3 undergoes the most significant effective strain, whereas point P1, located near the primary ingot periphery and in proximity to the pipe wall channel, is subject to the least strain due to the greater distance it must traverse to reach the pipe wall channel.

By comparing the strain amplitudes at different points induced by various tool designs, it is apparent that the 30° tapered tool exerts the highest strain, while the cylindrical tool exerts the least strain, as it was similarly depicted in Fig. 5.

Fig. 8b depicts the strain rates applied to various points using different FSE tools. The amplitude of the strain rate remains almost consistent for the same point with tapered tools. However, a notable difference is observed with the cylindrical tool. In contrast to the effective strain, the strain rate applied by the cylindrical tool is significantly higher than that applied by the taper tools. This indicates that while the cylindrical tool induces less deformation, the rate of this deformation is accelerated, occurring at a higher speed. The peak strain rate for the taper tools does not exceed 10 1/s, whereas it reaches almost 40 1/s for the cylindrical tool.

The microstructures of the tube walls produced by three different tool designs are shown in Fig. 9. All of the OM images are taken 20 mm above the conjunction of the taper section and tube wall as shown by the letter “e” in Fig. 1a. It is clear that the silicone precipitate size and void size in the sample created with the cylindrical tool are the largest, whereas they are the smallest in the sample produced by the 30° taper tool. The average Si particle size is 2.2, 1.7, and 1.4 μm and the average porosity size is almost 5, 2.3, and 1.1 μm for cylindrical, 60° taper, and 30° taper tools, respectively. In addition, the number of porosities in the 30° taper tool is also less than the cylindrical tool. The result of higher strain applied by the 30° taper tool, is more elimination of porosities and more breakage of Si particles which is obvious in Fig. 9c. These superior microstructural characteristics could have a positive impact on the mechanical properties.

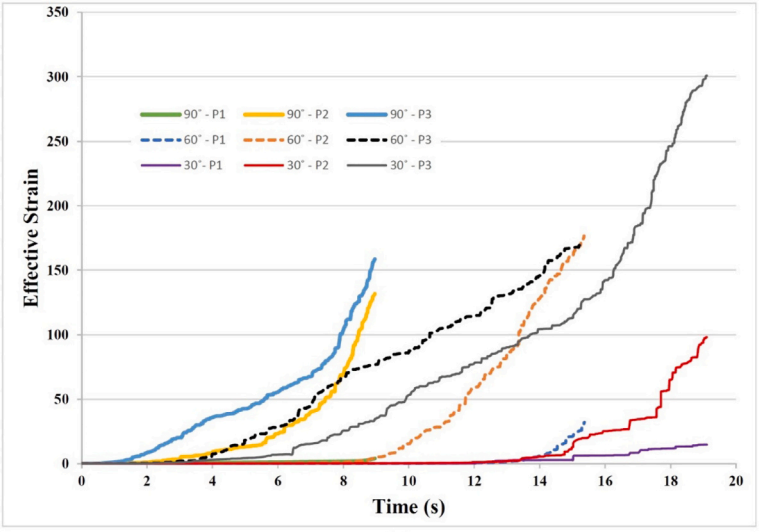

(a)

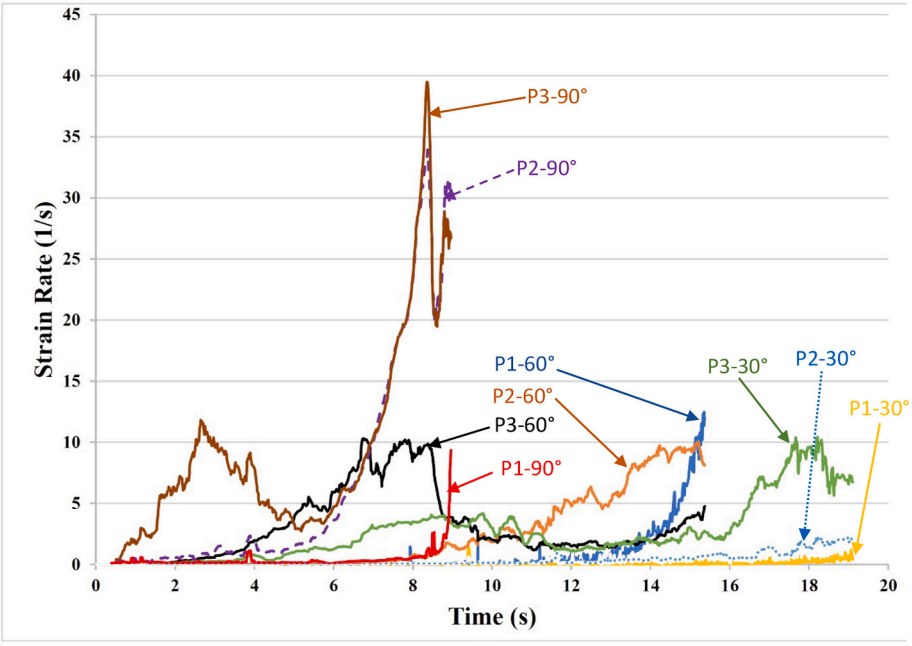

(b)

Fig. 8. The (a) effective strain and (b) strain rate, histories experienced by points P1-P3 for three designs of tool head.

From another perspective, while the high strain rate at lower temperatures is advantageous for material forming, resulting in a finer microstructure and increased strength [42], the cylindrical tool in this study failed to effectively eliminate porosity and break Si particles to the same extent as the tapered tools. Additionally, the study found that strain had a greater influence than strain rate.

4.6. Compressive strength

The compression test stress-strain curves of FSE specimens fabricated using various tool designs, including cylindrical and taper head tools, are illustrated in Fig. 10. The original as-cast material shows the Ultimate Compression Strength (UCS) of approximately 85 MPa, whereas it increased to 139 MPa for the FSE-manufactured sample employing a 30° taper angle tool. Despite the UCS for the sample created with a cylindrical head tool being lower at 117.2 MPa compared to the other FSE samples, its strength surpasses that of the original as-cast material. This indicates that the friction stir extrusion enhances the alloy strength by rectifying casting defects. As discussed in the sections on material flow and strain assessment, a higher strain, coupled with a smooth material flow pattern during the process, aids in eliminating pores and discontinuities present in the base material, thereby enhancing material integrity [43]. This same rationale places the UCS of the FSE sample produced with a 30° taper angle tool in a superior position. Although the cylindrical tool exerts greater forging force and strain rate, it appears that the extended application of higher strain over time by the 30° taper angle tool is more effective in enhancing material strength.

In Fig. 10, it is also evident that the strain of the FSE processed samples shows a significant improvement compared to the as-cast sample. Moreover, the strain observed in the sample produced using a 30° taper angle tool surpasses that of the other processed samples. The ductility of the LM13 as-cast alloy is enhanced through microstructural alterations, such as the transformation of needle-like structures into finer circular Si particles and the elimination of casting imperfections

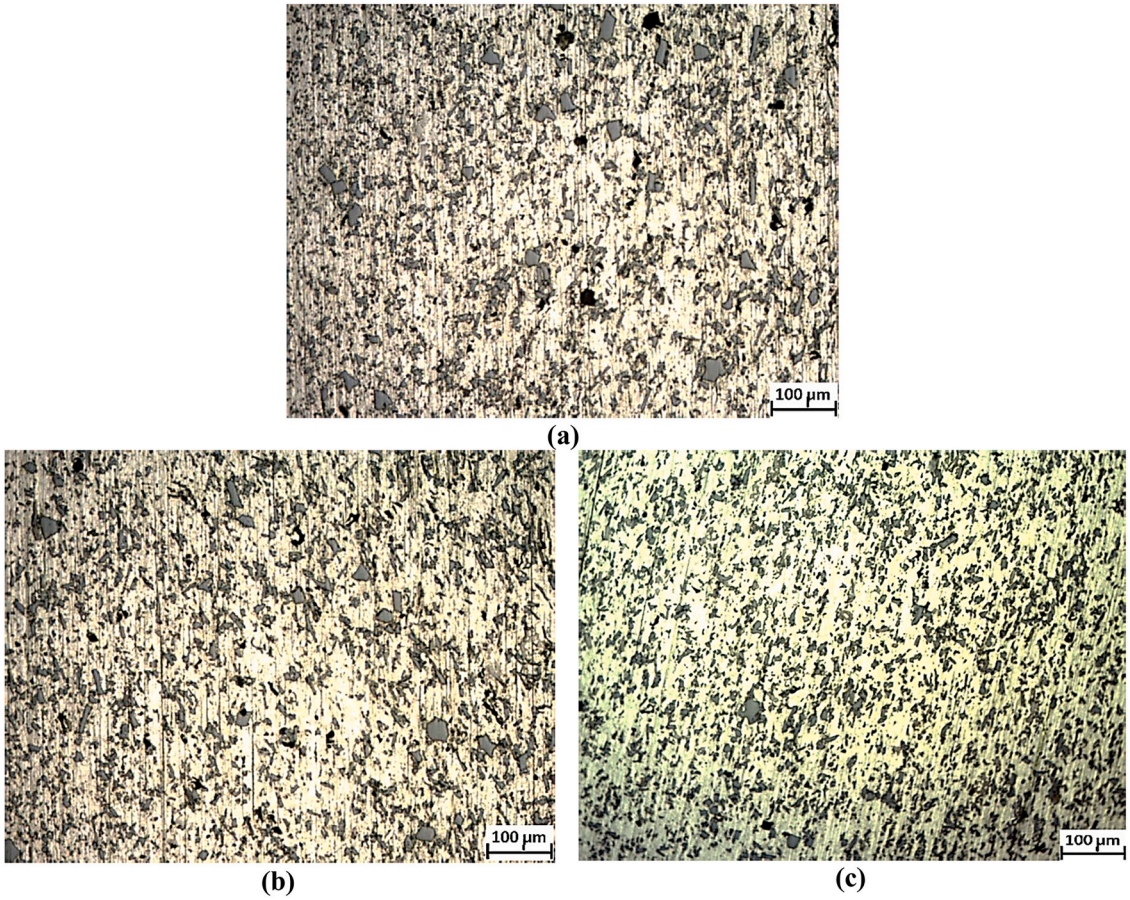

Fig. 9. Optical microscopy images taken from pipe walls of the produced samples by different FSE tools with (a) cylindrical, (b) 60° taper, and (c) 30° taper head; showing the porosities and Si particle size.

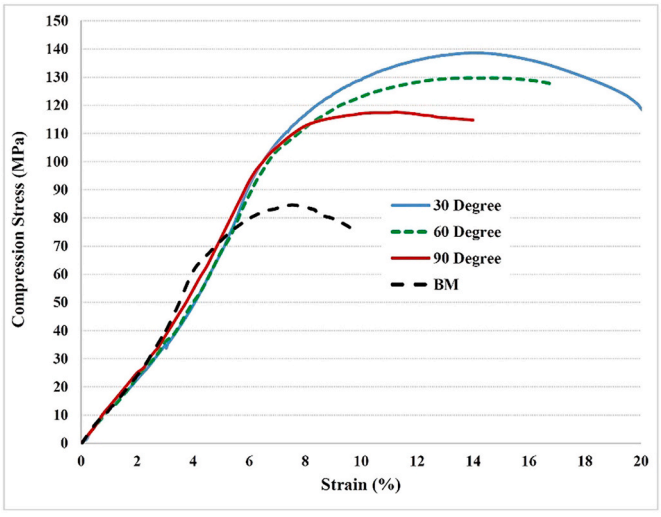

Fig. 10. Comparing the compression strength for base metal and FSE samples manufactured by using different tool profiles with cylindrical and taper angles of 30 and 60°.

present in the original material. Given the superior performance of the 30° taper angle tool in these aspects, it is anticipated that the strain achieved in the compression test by this particular specimen will be notably higher.

By comparing the impact of FSE on the mechanical properties of as-cast material with that of the other SPD processes, Lapovok et al. [44] succeeded in improving the compression strength of the as-cast Mg–Y–Zn alloy from ~315 MPa in the heat-treated sample to ~570 MPa in the sample produced by 4 passes of Equal Channel Angular Processing (ECAP). To achieve this improvement, they annealed the samples at 450 and 500 °C for 15–30 min. However, this led to a decrease in ductility from 35 % in the as-cast heat-treated sample to lower levels in the ECAPed samples. Similarly, Ma et al. [45] increased the strength and ductility of the Al-11%Si as-cast alloy from 215 MPa and 7 % to almost 250 MPa and 20 % by applying 32 passes of RD-ECAP process. According to Rogachev et al. [46], applying 3 passes of the high-pressure torsion (HPT) process improved the strength of the as-cast Al–Ca–Mn–Fe alloy from 160 MPa to almost 670 MPa. However, applying 5 passes of HPT reduced the strength to 150 MPa.

It is well understood that the strain values differ among various SPD techniques. Typically, the strain values are around 1–5 for ECAP and HPT processes [47–51], while they range from 10 to 300 mm/mm for friction stir-based processes, as reported in the literature [52–54]. The high amount of strain applied by the FSE process, coupled with flaw dissipation, can facilitate the production of composite parts with a uniform distribution of reinforcing particles [4,55].

5. Conclusions

This research utilized three different tool head designs for the FSE of LM13 aluminum alloy. The resulting samples were examined for microstructure and mechanical properties. A numerical simulation analyzed FSE performance, focusing on strain and temperature contours, material flow patterns, and the histories of force, torque, strain, and strain rate. The analysis aimed to explain the observed

microstructure and mechanical characteristics of the samples. The results indicate that:

1- In the FSE region, 6–10 mm above the junction of the taper head and tube wall, peak strain and temperatures were recorded, with maximum temperatures of 460 °C, 440 °C, and 410 °C for the 30° taper, 60° taper, and cylindrical tools, respectively.
2- The tool head design significantly affects the axial force required for the FSE process, with cylindrical tools requiring 4–5 times more force than tapered tools. Forces for the 30° and 60° taper tools are similar because the higher temperature of the 30° taper is offset by its larger swept material.
3- The strain from the 30° taper tool is notably higher than from the others, reducing porosity and silicone precipitate size in LM13 alloy, thus significantly enhancing the mechanical strength of the produced pipe.
4- The strain rate from the cylindrical tool is significantly higher at about 40 1/s, compared to below 10 for the taper tools. However, the cylindrical tool is less effective at eliminating porosity and breaking Si particles. Consequently, the compressive strength is highest for the 30° taper tool at 138.7 MPa, followed by 130 MPa for the 60° taper and 117.2 MPa for the cylindrical tool.
5- The material flow pattern varies between tools: in the cylindrical tool, material moves from the periphery to the inside of the ingot, while in tapered tools, it flows from the center toward the pipe wall channel.
6- The 30° taper head tool, with its combination of high temperature, high strain, and low force, along with superior mechanical properties, is established as the optimal choice for the FSE process.

CRediT authorship contribution statement

Parviz Asadi: Writing – original draft, Validation, Investigation, Formal analysis, Data curation, Conceptualization. **Mostafa Akbari:** Writing – original draft, Software, Formal analysis, Data curation. **Tomasz Sadowski:** Writing – review & editing, Validation, Supervision, Formal analysis. **Yaghuob Dadgar Asl:** Software, Data curation. **Naghdali Choupani:** Writing – review & editing, Investigation, Formal analysis. **Fevzi Bedir:** Writing – review & editing, Investigation, Data curation.

Declaration of competing interest

The authors declare that they have no known competing financial interests or personal relationships that could have appeared to influence the work reported in this paper.

Acknowledgements

Parviz Asadi acknowledges “TUBITAK 2221 program for visiting scientists on sabbatical leave (2023/6)” to visit Gebze Technical University, Turkiye.

This work was funded under the grant “Subvention for Science” by the Ministry of Education and Science of the Republic of Poland (T. Sadowski) - project No. FD-20/IL-4/046.

References

[1] Zheng Q, et al. Achieving superior grain refinement efficiency for Al–Si casting alloys through a novel Al–La–B grain refiner. J Mater Res Technol 2024;30:52–60.
[2] Zhao Z, et al. Insights into the dual effects of Ti on the grain refinement and mechanical properties of hypoeutectic Al–Si alloys. J Mater Sci Technol 2024;189:44–59.
[3] Noga P, Skrzekut T, Wedrychowicz M. Microstructure and mechanical properties of Al-Si alloys produced by rapid solidification and hot extrusion. Materials (Basel) 2023;16(15).
[4] Akbari M, Asadi P, Sadowski T. A review on friction stir welding/processing: numerical modeling. Materials (Basel) 2023;16(17).
[5] Szymczak T, et al. Characteristics of Al-Si alloys with high melting point elements for high pressure die casting. Materials (Basel) 2020;13(21).
[6] Shabestari SG, et al. Interplay among coating thickness, strip size, and thermal and solidification characteristics in A356 lost foam casting alloy. Metall Mater Trans B 2017;48(5):2304–15.
[7] Cast aluminum alloy datasheets. In: Properties and selection of aluminum alloys; 2019. p. 507–12.
[8] Asadi P, et al. Recycling of brass chips by sustainable friction stir extrusion. J Clean Prod 2023;418.
[9] Asadi P, et al. Characterization of the influence of rotational and traverse speeds on the mechanical and microstructural properties of wires produced by the FSBE method. Strength of Materials 2022;54(2):318–30.
[10] Asadi P, Akbari M. Numerical modeling and experimental investigation of brass wire forming by friction stir back extrusion. Int J Adv Manuf Technol 2021;116:3231–45.
[11] Akbari M, Asadi P. Optimization of microstructural and mechanical properties of brass wire produced by friction stir extrusion using Taguchi method. Proceedings of the Institution of Mechanical Engineers, Part L: Journal of Materials: Design and Applications 2021;235(12):2709–19.
[12] Baffari D, et al. Friction stir extrusion to recycle aluminum alloys scraps: energy efficiency characterization. J Manuf Process 2019;43:63–9.
[13] Buffa G, et al. Improving the industrial efficiency of recycling aluminum alloy chips using friction stir extrusion: thin wires production process. Int J Precis Eng Manuf-Green Technol 2024;11:1133–46.
[14] Swarnkar R, Karmakar S, Pal SK. An investigation of bimetallic tube fabrication through a novel friction stir extrusion based technology for automotive applications. Materials Today Communications 2023:35.
[15] Abdi Behnagh R, et al. Predicting microstructure evolution for friction stir extrusion using a cellular automaton method. Model Simul Mater Sci Eng 2019:**27**(3).
[16] Immanuel RJ, Panigrahi SK. Influence of cryorolling on microstructure and mechanical properties of a cast hypoeutectic Al–Si alloy. Mater Sci Eng A 2015;640:424–35.
[17] Qi Y, et al. Generation and healing of porosity in high purity copper by high-pressure torsion. Mater Charact 2018;145:1–9.
[18] Das A. Stress/strain induced void? Archives of Computational Methods in Engineering 2020;28(3):1795–852.
[19] Akbari M, Ezzati M, Asadi P. Investigation of the effect of tool probe profile on reinforced particles distribution using experimental and CEL approaches. International Journal of Lightweight Materials and Manufacture 2022;5(2):213–23.
[20] Asadi P, Mirzaei M. Material flow modeling for the DSFSW of magnesium alloy. The Journal of Strain Analysis for Engineering Design 2020;56(5):275–90.
[21] Baffari D, et al. Process mechanics in friction stir extrusion of magnesium alloys chips through experiments and numerical simulation. J Manuf Process 2017;29:41–9.
[22] Asadi P, Akbari M, Karimi-Nemch H. 12 - simulation of friction stir welding and processing. In: Givi MKB, Asadi P, editors. Advances in friction-stir welding and processing. Woodhead Publishing; 2014. p. 499–542.
[23] Akbari M, Asadi P. Effects of different cooling conditions on friction stir processing of A356 alloy: numerical modeling and experiment. Proc Inst Mech Eng C J Mech Eng Sci 2021;236(8):4133–46.
[24] Tutunchilar S, et al. Simulation of material flow in friction stir processing of a cast Al–Si alloy. Mater Des 2012;40:415–26.
[25] Hangai Y, et al. Drop weight impact behavior of Al-Si-Cu alloy foam-filled thin-walled steel pipe fabricated by friction stir Back extrusion. J Mater Eng Perform 2016;26(2):894–900.
[26] Al-Buainain M, et al. Influence of microstructure on the mechanical and corrosion response of a friction stir-extruded WE43 magnesium rod. Metals 2023;13(2).
[27] Dong G, et al. Process optimization of A356 aluminum alloy wheel hub fabricated by low-pressure die casting with simulation and experimental coupling methods. J Mater Res Technol 2023;24:3118–32.
[28] Jia D-S, et al. Effects of equal channel angular pressing and further cold upsetting process to the kinetics of precipitation during aging of 7050 aluminum alloy. J Mater Res Technol 2023;26:5126–40.
[29] Ebrahimi M, Wang Q. Accumulative roll-bonding of aluminum alloys and composites: an overview of properties and performance. J Mater Res Technol 2022;19:4381–403.
[30] Akbari M, Asadi P, Asiabaraki HR. Investigation of wear and microstructural properties of a356/ TIC composites fabricated by FSP. Surf Rev Lett 2022;29(10):2250130.
[31] Morozova I, et al. Precipitation phenomena in impulse friction stir welded 2024 aluminium alloy. Mater Sci Eng A 2022:852.
[32] dos Santos JF, et al. Understanding precipitate evolution during friction stir welding of Al-Zn-Mg-Cu alloy through in-situ measurement coupled with simulation. Acta Mater 2018;148:163–72.
[33] Sozhamannan GG, Prabu SB. Influence of interface compounds on interface bonding characteristics of aluminium and silicon carbide. Mater Charact 2009;60(9):986–90.
[34] Jones DRH, Ashby MF. Continuum aspects of plastic flow. In: Engineering materials. *1*; 2019. p. 179–93.
[35] Akbari M, Aliha MRM, Berto F. Investigating the role of different components of friction stir welding tools on the generated heat and strain. Forces in Mechanics 2023;10:100166.

[36] Rouzbeh A, Sedighi M, Hashemi R. Effects of strain path on the microstructure, tensile properties, and formability of Al/Mg roll-bonded sheets. J Mater Res Technol 2023;23:5318–28.
[37] Markovsky PE, et al. Effect of strain rate on microstructure evolution and mechanical behavior of titanium-based materials. Metals 2020;10(11).
[38] Motavallian P, Rabiee SM, Jamshidi Aval H. Evaluation of AZ91-bioactive glass composites produced by the friction stir back extrusion technique. J Manuf Process 2023;101:1551–80.
[39] Mehdipour M, Jamshidi Aval H. Effect of friction stir back extrusion rotational speed on microstructure, mechanical properties, and corrosion behaviour of AZ91-Ca alloy. J Mater Res Technol 2023;25:4441–56.
[40] Samanta A, et al. Microstructure-refinement–driven enhanced tensile properties of high-pressure die-cast A380 alloy through friction stir processing. J Manuf Process 2022;78:352–62.
[41] Talebi M, Asadi P, Akbari M. Friction stir extrusion and mechanical alloying of LM13 casting ingot to produce LM28 tubes. J Mater Res Technol 2023;27:6672–87.
[42] Chai F, et al. Effect of strain rates on mechanical behavior, microstructure evolution and failure mechanism of extruded-annealed AZ91 magnesium alloy under room-temperature tension. J Mater Res Technol 2023;27:4644–56.
[43] Lakshminarayanan AK, et al. Decisive influence of critical process parameters on the microstructure and tensile properties of friction stir back extruded magnesium alloy tubes. J Manuf Process 2022;73:207–19.
[44] Lapovok R, et al. Enhancement of properties in cast Mg–Y–Zn rod processed by severe plastic deformation. Mater Sci Eng A 2014;615:198–207.
[45] Ma A, et al. Effect of severe plastic deformation on tensile properties of a cast Al–11mass% Si alloy. Mater Sci Eng A 2005;395(1–2):70–6.
[46] Rogachev SO, et al. Improvement of strength–ductility balance of Al–Ca–Mn–Fe alloy by severe plastic deformation. Mater Lett 2023;349.
[47] Alateyah AI, et al. Effect of ECAP die angle on the strain homogeneity, microstructural evolution, crystallographic texture and mechanical properties of pure magnesium: numerical simulation and experimental approach. J Mater Res Technol 2022;17:1491–511.
[48] Djavanroodi F, et al. Designing of ECAP parameters based on strain distribution uniformity. Progress in Natural Science: Materials International 2012;22(5): 452–60.
[49] Nugmanov D, et al. Equivalent strain distribution at high pressure torsion extrusion of pure copper: finite element modeling and experimental validation. J Mater Process Technol 2023;315.
[50] Jonas JJ, Ghosh C, Toth LS. The equivalent strain in high pressure torsion. Mater Sci Eng A 2014;607:530–5.
[51] Gunderov DV, et al. Slippage during high-pressure torsion: accumulative high-pressure torsion—overview of the latest results. Metals 2023;13(8).
[52] Li Z, et al. Strain accumulation and microstructural evolution during friction stir welding of pure magnesium. Frontiers in Materials 2020:7.
[53] Bajaj D, et al. Flow, process forces and strains during friction stir welding: a comprehensive first principle approach. Proc Inst Mech Eng B J Eng Manuf 2020; 235(5):912–24.
[54] Jarrah OM, Nazzal MA, Darras BM. Numerical modeling and experiments of Friction Stir Back Extrusion of seamless tubes. CIRP J Manuf Sci Technol 2020;31: 165–77.
[55] Raja S, et al. A review on nanomaterials reinforcement in friction stir welding. J Mater Res Technol 2020;9(6):16459–87.